Supplementary Information for

Non-Equilibrium Formation of the Elusive Dibridged Diboranyl (B_2H_5) Radical and Boranes in Low-Temperature Diborane Ices

Jia Wang,[1,2] Joshua H. Marks,[1,2] Chaojiang Zhang,[1,2] Andrew M. Turner,[1,2] Mason McAnally,[1,2] Miori Nogamida,[1,2,3] Ralf I. Kaiser[1,2*]

[1] *W. M. Keck Research Laboratory in Astrochemistry, University of Hawaii at Manoa, Honolulu, HI 96822, United States*

[2] *Department of Chemistry, University of Hawaii at Manoa, Honolulu, HI 96822, United States*

[3] *Present address: Chuo University, 1-13-27 Kasuga, Bunkyo-ku, Tokyo 112-8551, Japan*

[*]Corresponding Author:

Ralf I. Kaiser, ralfk@hawaii.edu

Experimental

All experiments were conducted in a stainless steel ultrahigh vacuum chamber, achieving pressures of a few 10^{-11} Torr using magnetically levitated turbomolecular pumps (Osaka, TG1300MUCWB and TG420MCAB) backed by an oil-free scroll pump (XDS35i, BOC Edwards).[1,2] A polished silver substrate was attached to an oxygen-free copper cold head and cooled to 5.0 ± 0.2 K by a closed-cycle helium refrigerator (Sumitomo Heavy Industries, RDK-415E). The substrate was translated in the horizontal and vertical directions via a rotatable flange coupled with an adjustable bellows. Diborane (B_2H_6, Sigma-Aldrich, 10% in hydrogen (H_2)) and diborane-d_6 (B_2D_6, Sigma-Aldrich, 10% in deuterium (D_2)) were introduced into the main chamber via a glass capillary array at a pressure of 1.3×10^{-7} Torr and deposited onto the cold substrate at 5 K. The growth of diborane and diborane-d_6 ices was monitored during deposition using laser interferometry[3] and reached four fringes, corresponding to an ice thickness of 950 ± 100 nm (Table S3), based on an estimated refractive index of 1.34 for diborane ice. After deposition, the ices were heated from 5 to 40 K at a rate of 2 K min^{-1} to remove the hydrogen or deuterium gas from the ices. To monitor chemical changes in the ices, infrared spectra were collected at a reflection angle of 45° over the range of 6000–500 cm^{-1} before, during, and after irradiation using a Fourier-transform infrared (FTIR) spectrometer (Thermo Electron, Nicolet 6700). The FTIR spectrometer was operated in absorption-reflection-absorption mode at a resolution of 4 cm^{-1} with 220 scans per spectrum. The ices were then irradiated at 40 K with a 5 keV electron beam generated by an electron gun (SPECS, EQ PU-22) at a current of 125 nA for 120 minutes, corresponding to a dose of 36 ± 5 eV $molecule^{-1}$ for diborane (Table S3). Utilizing a density of 0.447 g cm^{-3} for diborane,[4] the average electron penetration depth was determined to be 510 ± 50 nm based on Monte Carlo simulations performed with CASINO 2.42 software.[5] This penetration depth is much smaller than the ice thickness, thereby preventing interactions of electrons with the underlying silver substrate.

After irradiation, the ices were heated from 40 to 320 K at a rate of 1 K $minute^{-1}$ undergoing temperature-programmed desorption (TPD). During TPD, pulsed (30 Hz) vacuum ultraviolet (VUV) photons were used to ionize subliming gas-phase molecules, and the resulting ions were detected with a reflectron time-of-flight mass spectrometer (Jordan TOF Products, Inc.) equipped with a dual microchannel plate (MCP) detector. VUV photons at 9.34 eV were produced via resonant four-wave mixing ($\omega_{VUV} = 2\omega_1 - \omega_2$) of two synchronized laser beams (ω_1, ω_2) generated by two dye lasers (Sirah, Cobra-Stretch) and two Nd:YAG lasers (Spectra-Physics, Quanta Ray

Pro 250-30 and Pro 270-30). To generate 9.34 eV light, an Nd: YAG laser pumped a Rhodamine 610/640 dye mixture to produce light at 606.948 nm, which was subsequently frequency-tripled to yield ω_1 = 202.316 nm. A second Nd: YAG laser pumped a stilbene 420 dye to generate ω_2 = 425.117 nm. The two beams were spatially and temporally overlapped in a nonlinear krypton (Kr) gas medium, producing VUV photons at 9.34 eV. The VUV photons were separated from the fundamental laser beams (ω_1, ω_2) using a biconvex lithium fluoride lens in an off-axis geometry and directed approximately 2 mm above the ice surface to photoionize molecules in the gas phase.[1,2] The resulting ion signals were amplified with a preamplifier (Ortec 9305), processed by a discriminator (Advanced Research Instruments Corp., F100-TD), and recorded using a multichannel scaler (FAST ComTec, MCS6A). During TPD, mass spectra were acquired with a 2 minute accumulation time (3600 sweeps) and a time bin width of 3.2 ns. Ion signals were corrected for fluctuations in VUV intensity measured during the TPD phase. Blank experiments were performed without electron irradiation on diborane and diborane-d_6 ices to verify that the detected signals originated from irradiation-induced processes.

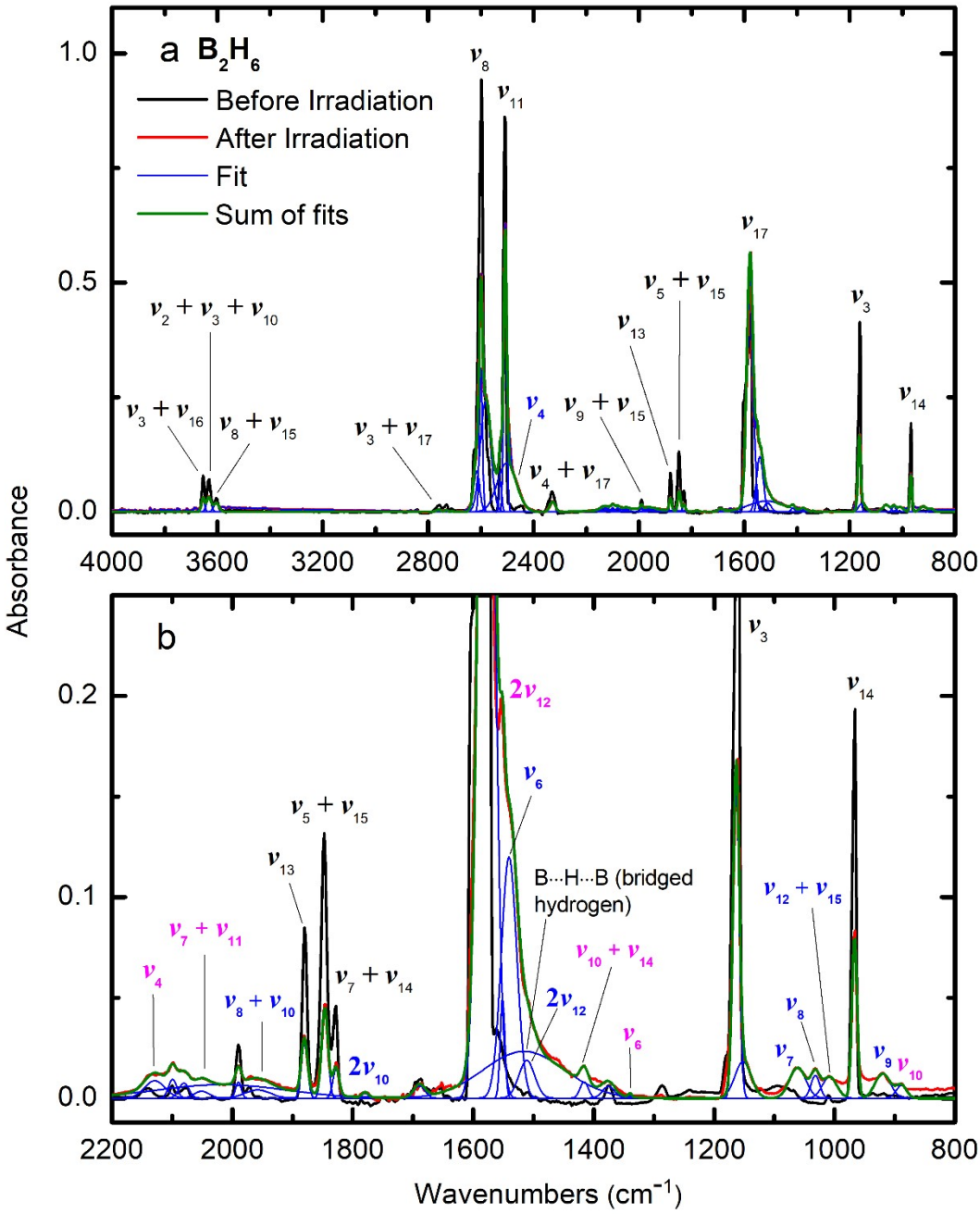

Figure S1. FTIR spectra of diborane (B_2H_6) ice at 40 K before (black) and after (red) irradiation at a current of 125 nA for 120 minutes (a). A magnified view of the 2200–800 cm^{-1} region showing new absorptions after irradiation (b). The green trace represents the sum of the individual fitted components of the infrared spectrum after irradiation. Detailed assignments are compiled in Table S1. The mono- and dibridged diboranyl (B_2H_5) radicals are labeled in blue and magenta, respectively.

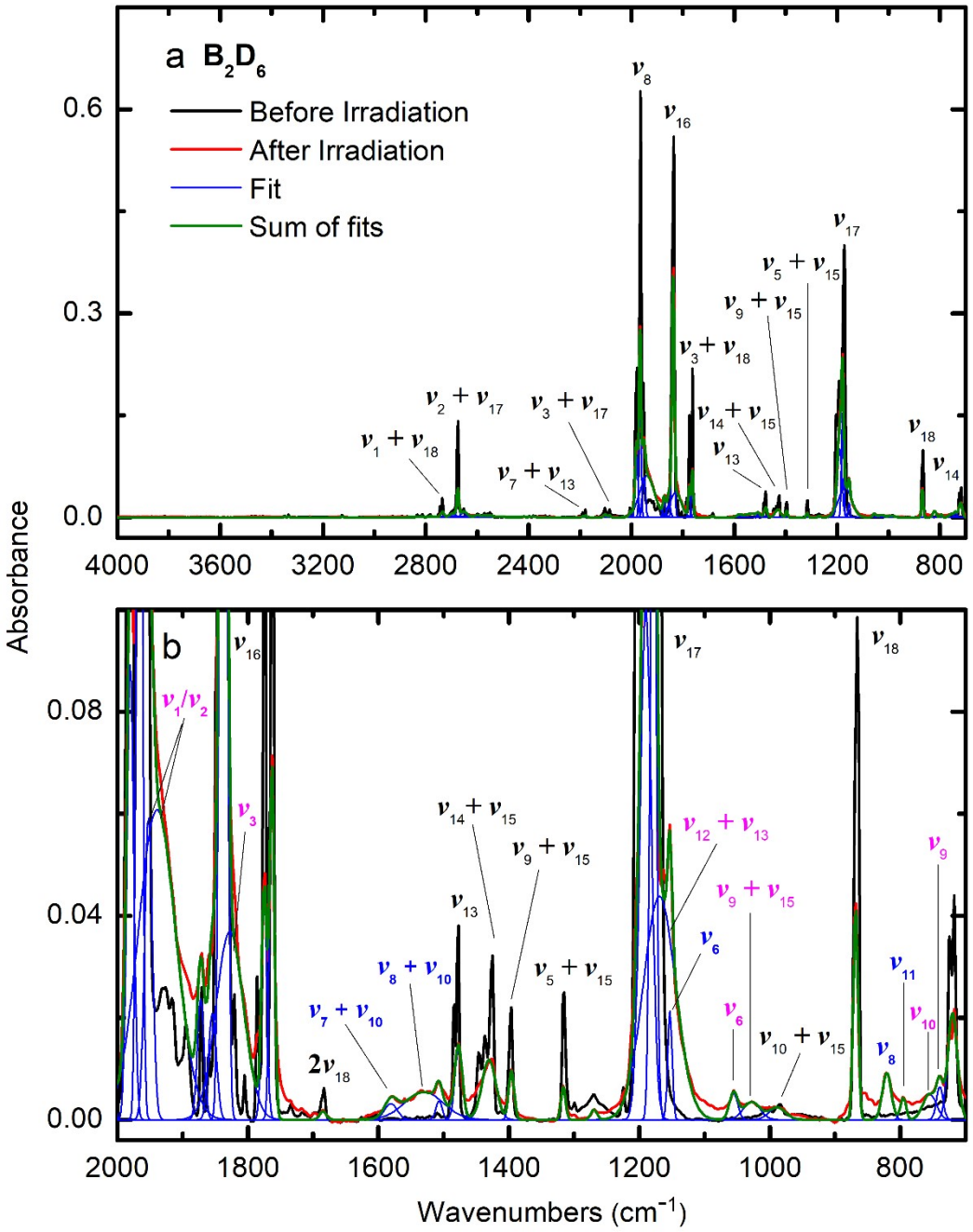

Figure S2. FTIR spectra of diborane-d_6 (B_2D_6) ice at 40 K before (black) and after (red) irradiation at a current of 116 nA for 120 minutes (a). A magnified view of the 2000–700 cm^{-1} region showing new absorptions after irradiation (b). The green trace represents the sum of the individual fitted components of the infrared spectrum after irradiation. Detailed assignments are compiled in Table S2. The mono- and dibridged diboranyl (B_2D_5) radicals are labeled in blue and magenta, respectively.

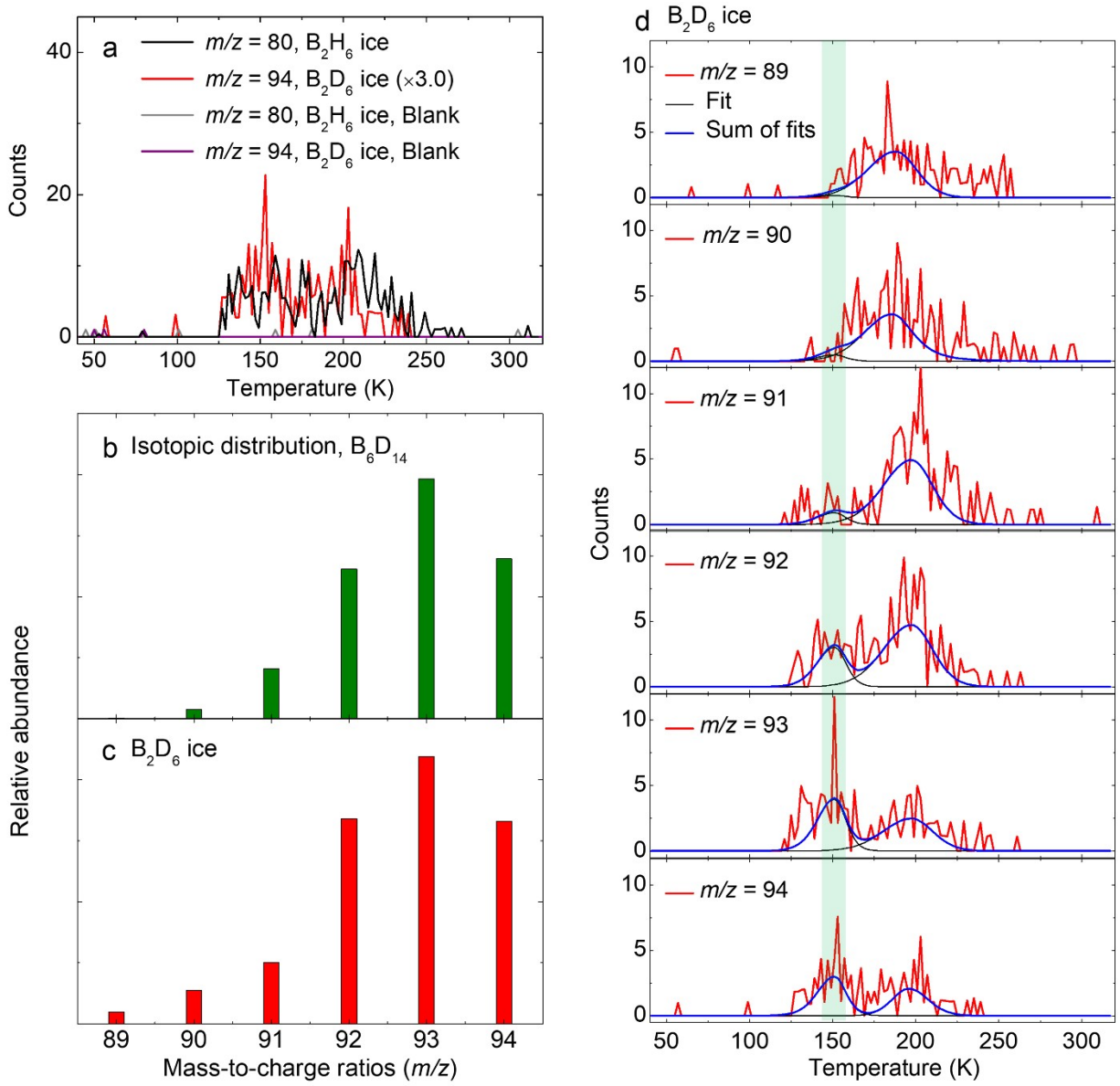

Figure S3. TPD profiles of *m/z* = 80 for diborane ice and *m/z* = 94 for diborane-d_6 ices recorded at 9.34 eV (a). Calculated isotopic distribution of B_6D_{14} (b) compared with experimental ion signals at *m/z* = 89–94 from irradiated diborane-d_6 ice (c), along with the corresponding TPD profiles (d). The solid blue lines indicate the total spectral fits, and the green shaded regions indicate peak positions assigned to B_6D_{14} isomers.

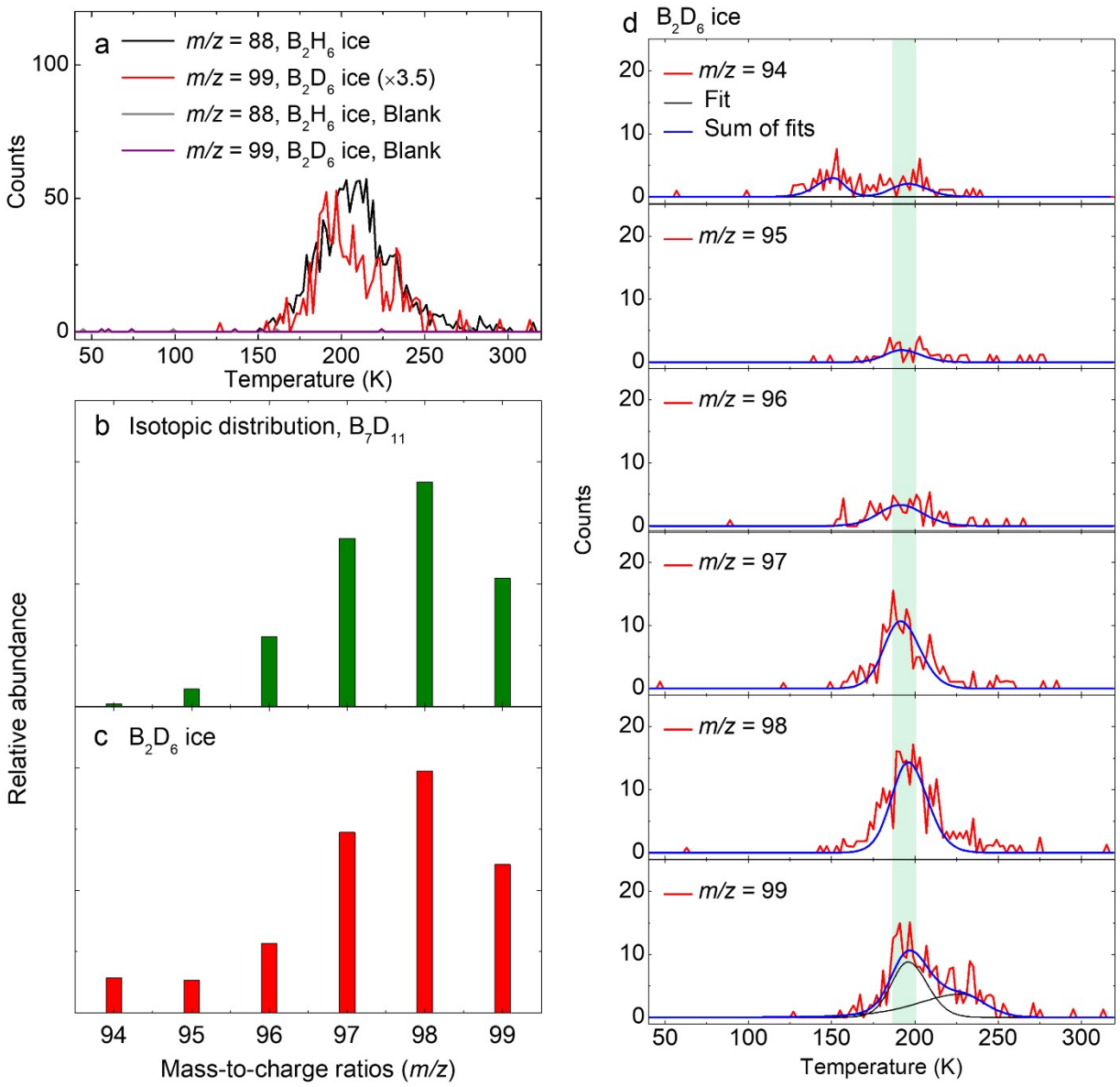

Figure S4. TPD profiles of *m/z* = 88 for diborane ice and *m/z* = 99 for diborane-d_6 ices recorded at 9.34 eV (a). Calculated isotopic distribution of B_7D_{11} (b) compared with experimental ion signals at *m/z* = 94–99 from irradiated diborane-d_6 ice (c), along with the corresponding TPD profiles (d). The solid blue lines indicate the total spectral fits, and the green shaded regions indicate peak positions assigned to B_7D_{11} isomers.

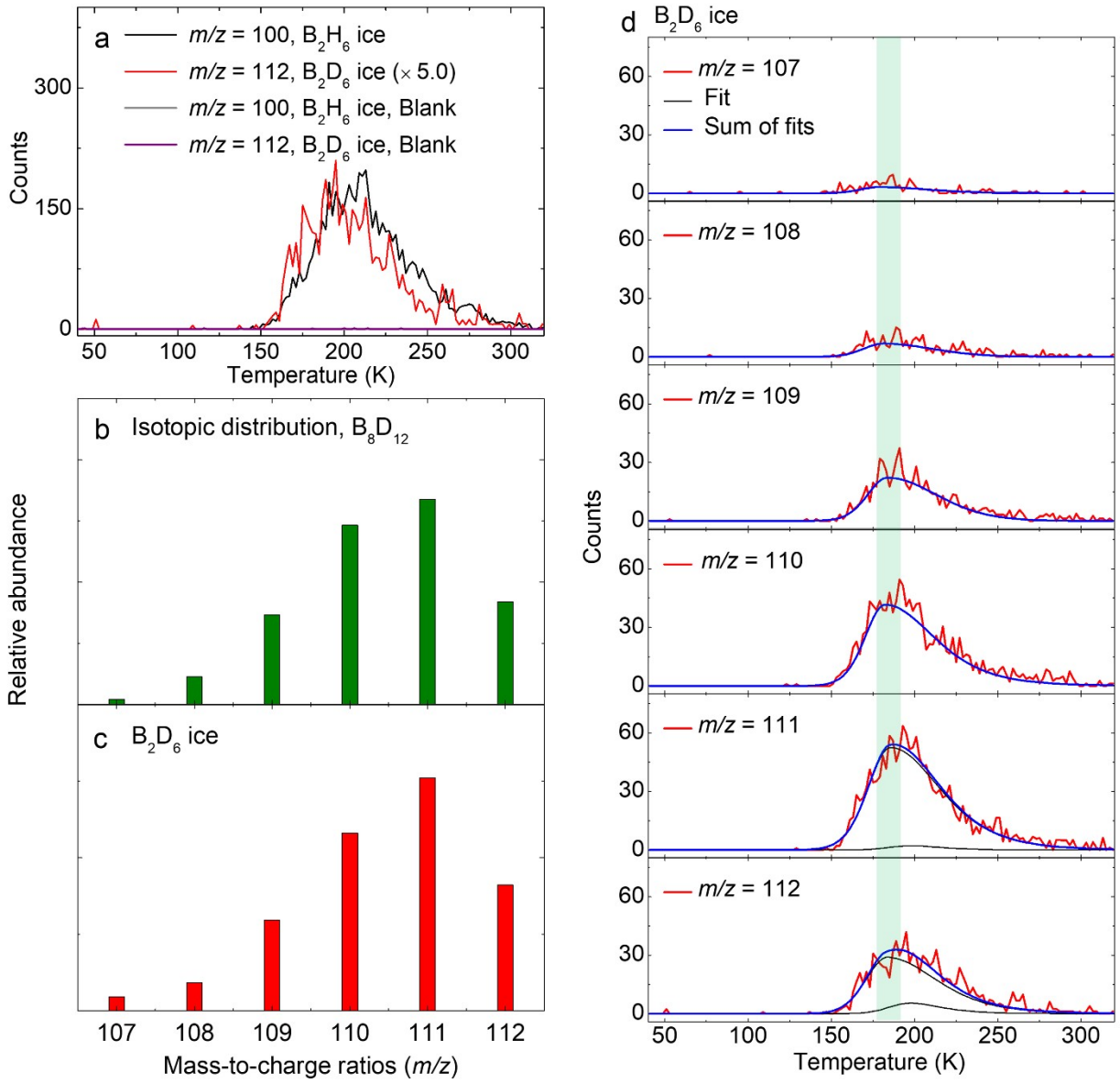

Figure S5. TPD profiles of m/z = 100 for diborane ice and m/z = 112 for diborane-d_6 ices recorded at 9.34 eV (a). Calculated isotopic distribution of B_8D_{12} (b) compared with experimental ion signals at m/z = 107–112 from irradiated diborane-d_6 ice (c), along with the corresponding TPD profiles (d). The solid blue lines indicate the total spectral fits, and the green shaded regions indicate peak positions assigned to B_8D_{12} isomers.

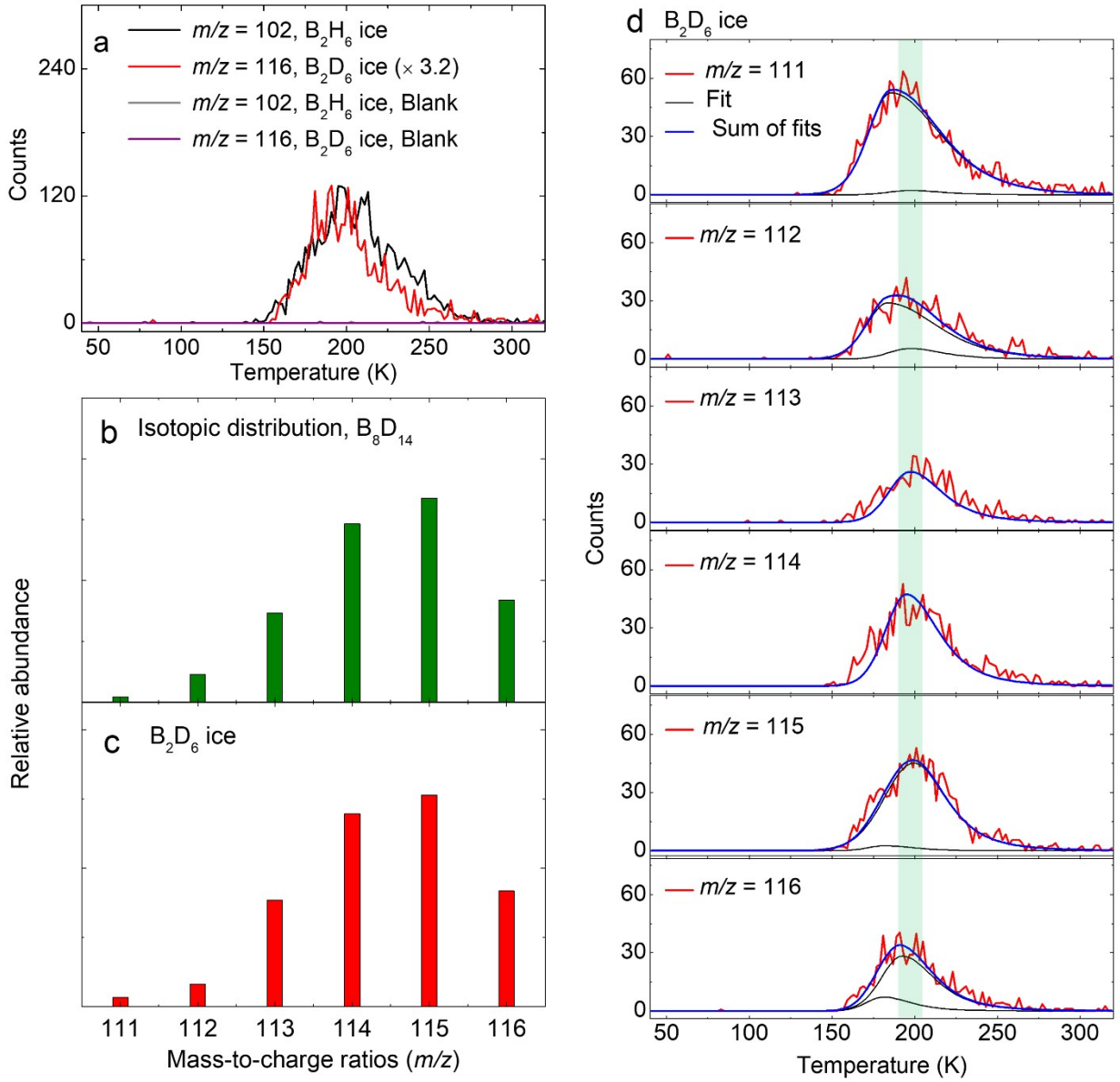

Figure S6. TPD profiles of *m/z* = 102 for diborane ice and *m/z* = 116 for diborane-d_6 ices recorded at 9.34 eV (a). Calculated isotopic distribution of B_8D_{14} (b) compared with experimental ion signals at *m/z* = 111–116 from irradiated diborane-d_6 ice (c), along with the corresponding TPD profiles (d). The solid blue lines indicate the total spectral fits, and the green shaded regions indicate peak positions assigned to B_8D_{14} isomers.

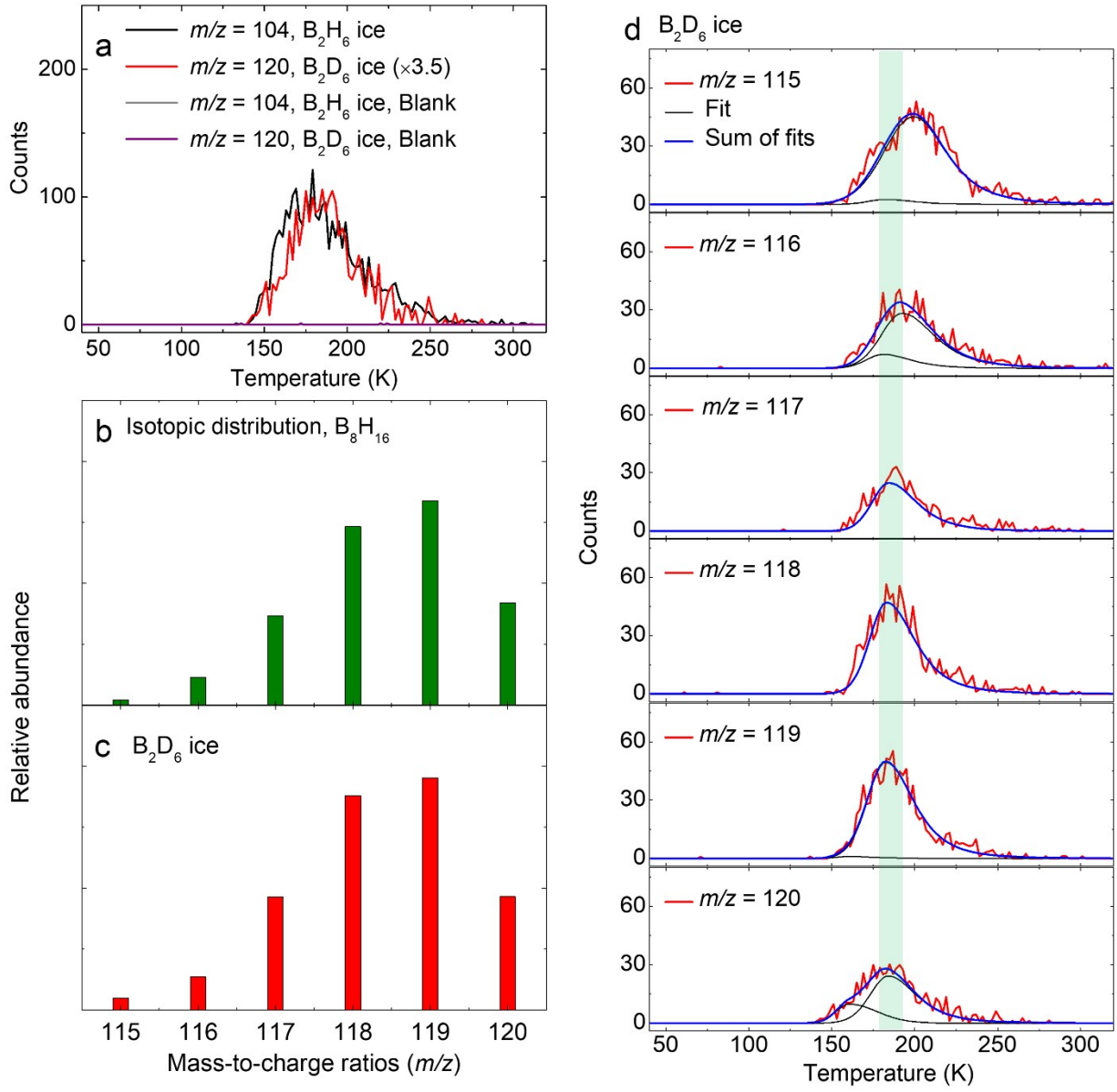

Figure S7. TPD profiles of *m/z* = 104 for diborane ice and *m/z* = 120 for diborane-d_6 ices recorded at 9.34 eV (a). Calculated isotopic distribution of B_8D_{16} (b) compared with experimental ion signals at *m/z* = 115–120 from irradiated diborane-d_6 ice (c), along with the corresponding TPD profiles (d). The solid blue lines indicate the total spectral fits, and the green shaded regions indicate peak positions assigned to B_8D_{16} isomers.

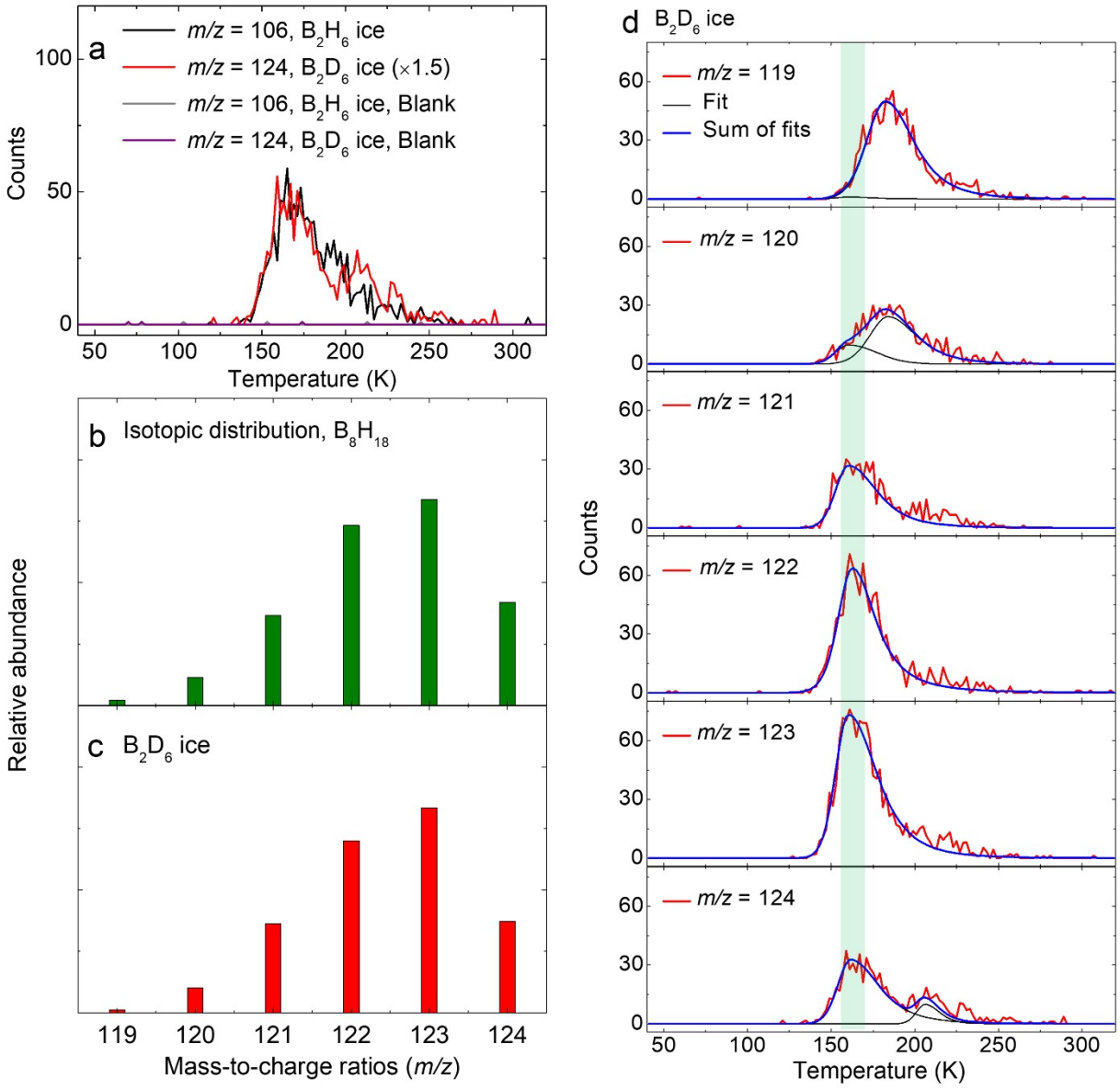

Figure S8. TPD profiles of *m/z* = 106 for diborane ice and *m/z* = 124 for diborane-d_6 ices recorded at 9.34 eV (a). Calculated isotopic distribution of B_8D_{18} (b) compared with experimental ion signals at *m/z* = 119–124 from irradiated diborane-d_6 ice (c), along with the corresponding TPD profiles (d). The solid blue lines indicate the total spectral fits, and the green shaded regions indicate peak positions assigned to B_8D_{18} isomers.

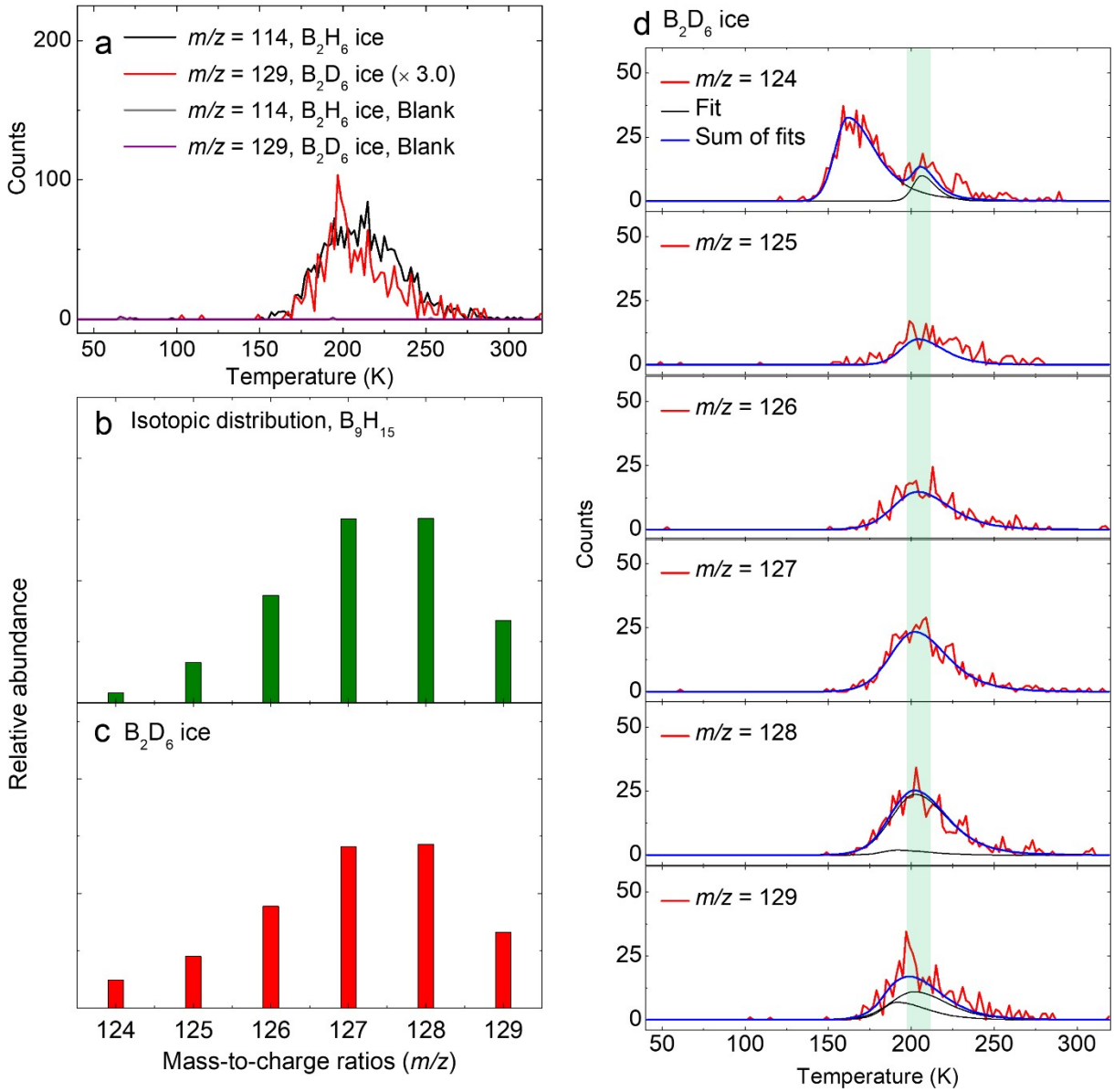

Figure S9. TPD profiles of m/z = 114 for diborane ice and m/z = 129 for diborane-d_6 ices recorded at 9.34 eV (a). Calculated isotopic distribution of B_9D_{15} (b) compared with experimental ion signals at m/z = 124–129 from irradiated diborane-d_6 ice (c), along with the corresponding TPD profiles (d). The solid blue lines indicate the total spectral fits, and the green shaded regions indicate peak positions assigned to B_9D_{15} isomers.

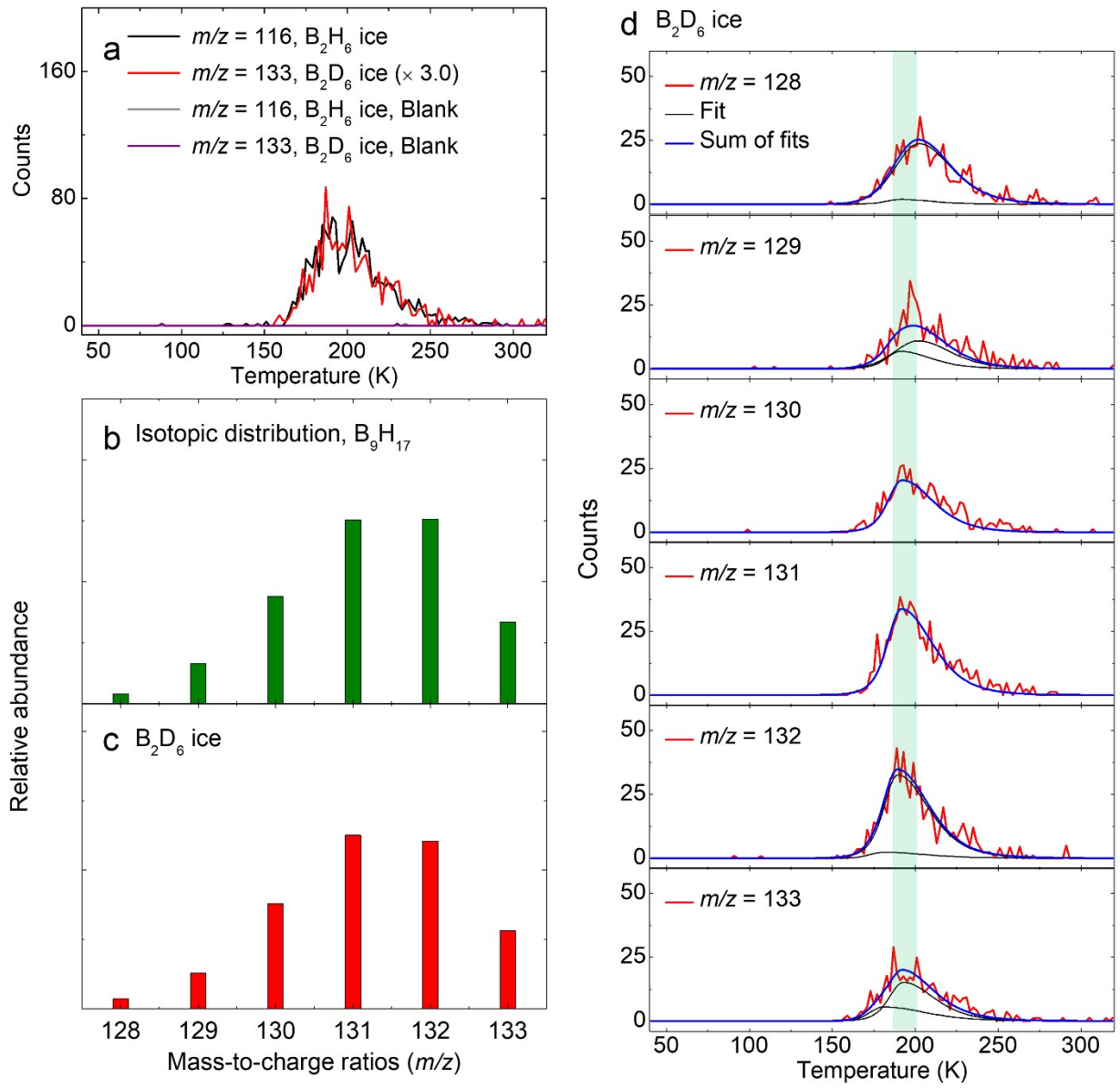

Figure S10. TPD profiles of $m/z = 116$ for diborane ice and $m/z = 133$ for diborane-d_6 ices recorded at 9.34 eV (a). Calculated isotopic distribution of B_9D_{17} (b) compared with experimental ion signals at m/z = 128–133 from irradiated diborane-d_6 ice (c), along with the corresponding TPD profiles (d). The solid blue lines indicate the total spectral fits, and the green shaded regions indicate peak positions assigned to B_9D_{17} isomers.

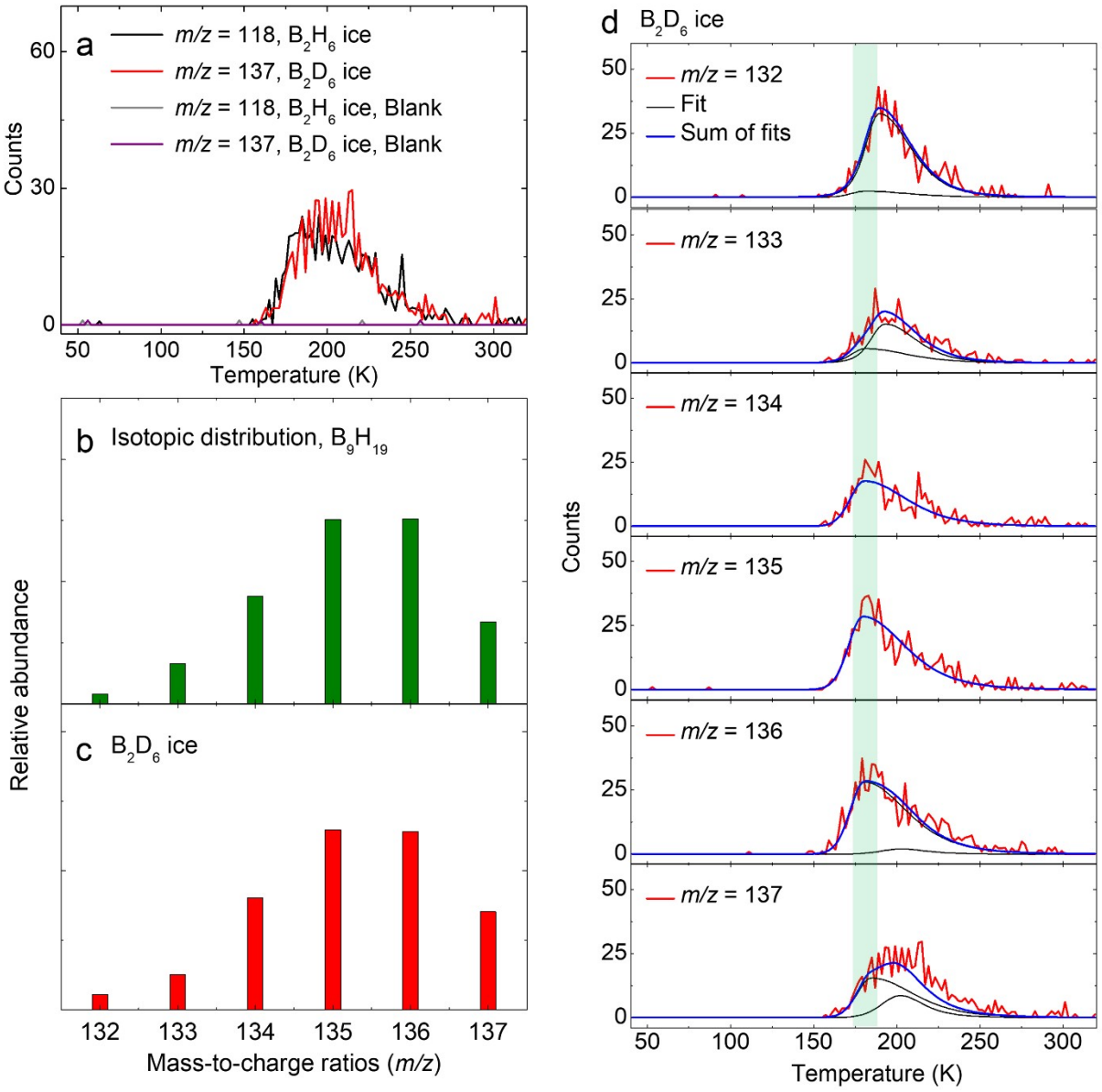

Figure S11. TPD profiles of $m/z = 118$ for diborane ice and $m/z = 137$ for diborane-d_6 ices recorded at 9.34 eV (a). Calculated isotopic distribution of B_9D_{19} (b) compared with experimental ion signals at m/z = 132–137 from irradiated diborane-d_6 ice (c), along with the corresponding TPD profiles (d). The solid blue lines indicate the total spectral fits, and the green shaded regions indicate peak positions assigned to B_9D_{19} isomers.

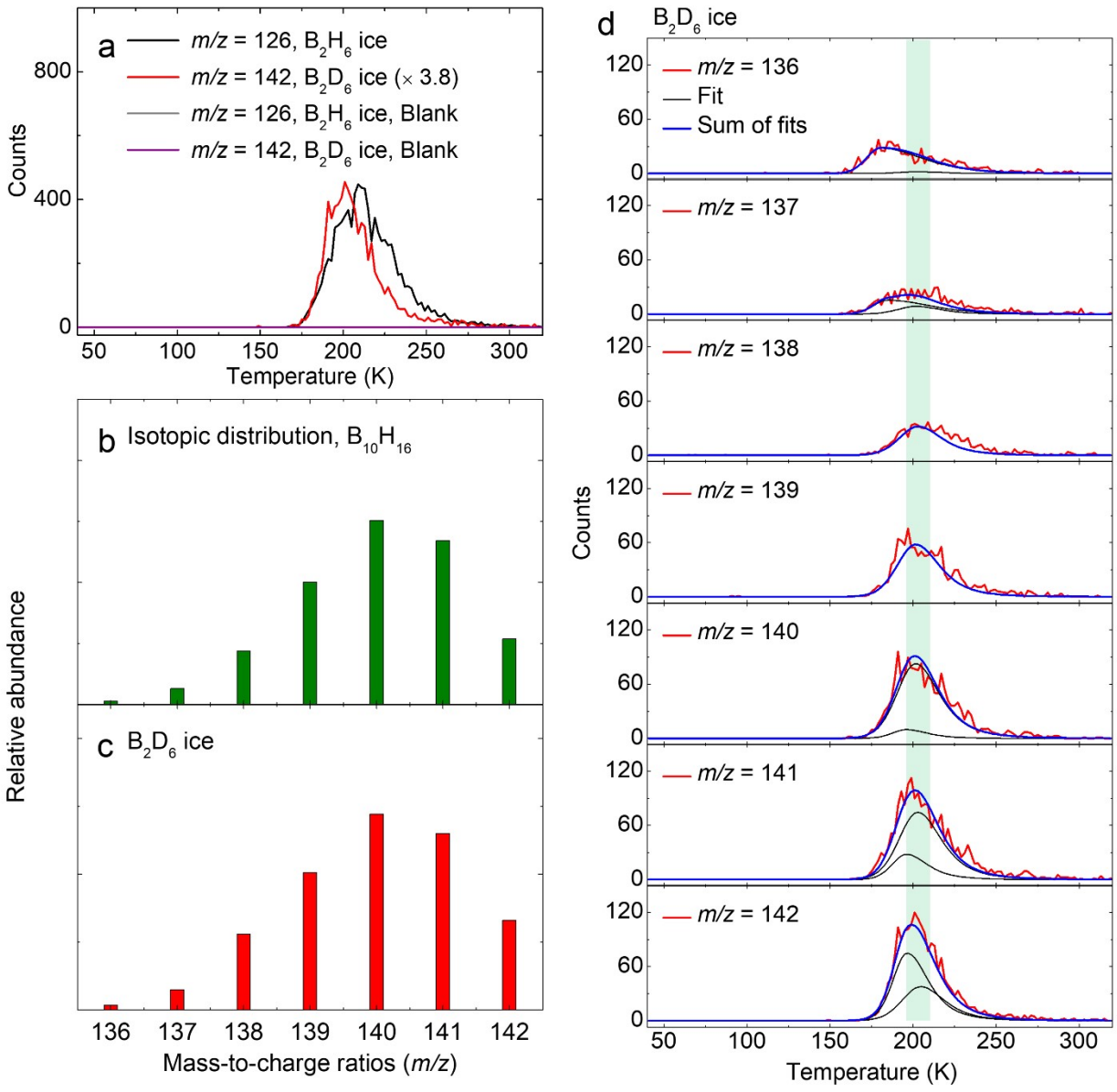

Figure S12. TPD profiles of *m/z* = 126 for diborane ice and *m/z* = 142 for diborane-d_6 ices recorded at 9.34 eV (a). Calculated isotopic distribution of $B_{10}D_{16}$ (b) compared with experimental ion signals at *m/z* = 136–142 from irradiated diborane-d_6 ice (c), along with the corresponding TPD profiles (d). The solid blue lines indicate the total spectral fits, and the green shaded regions indicate peak positions assigned to $B_{10}D_{16}$ isomers.

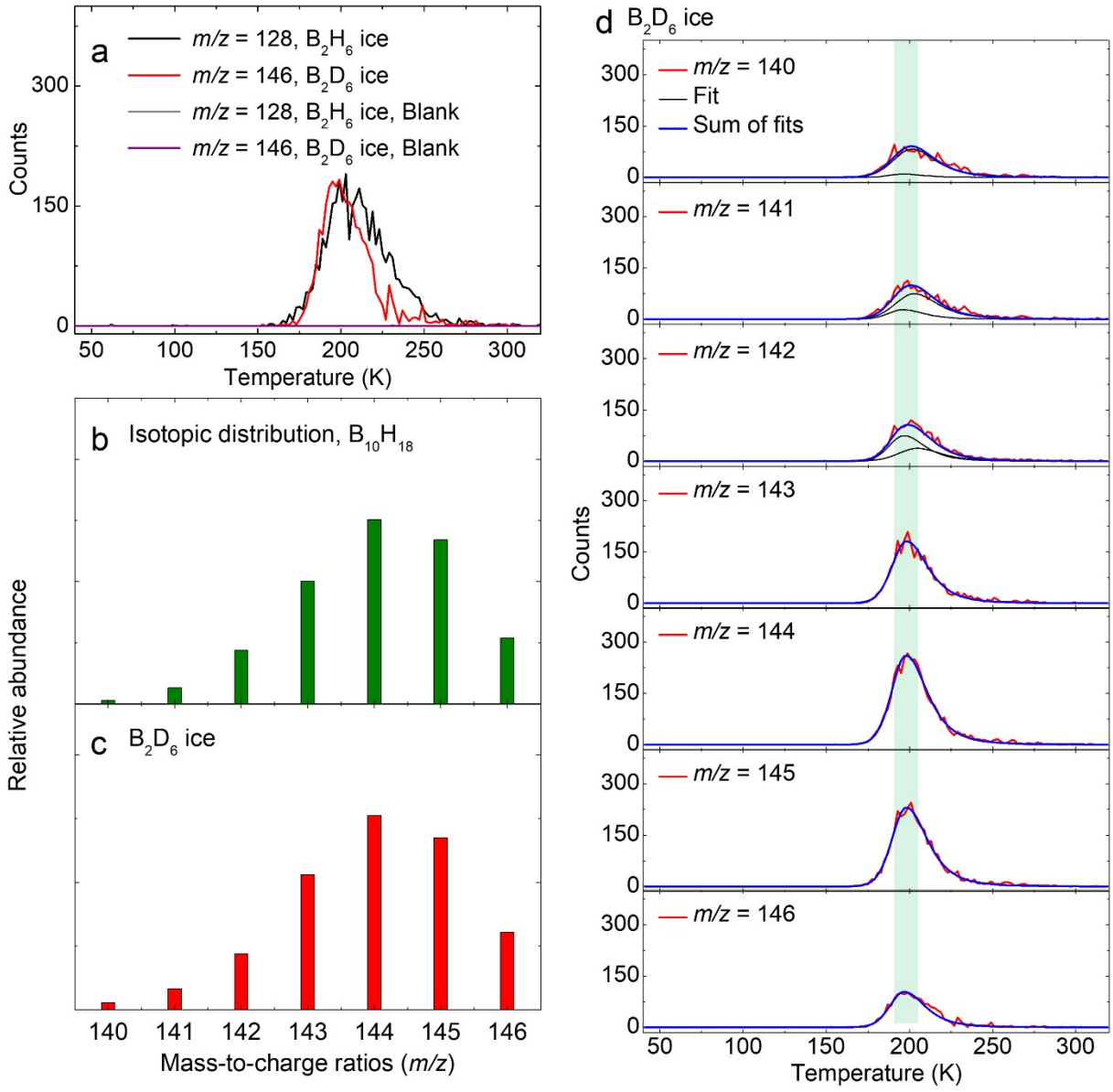

Figure S13. TPD profiles of *m/z* = 128 for diborane ice and *m/z* = 146 for diborane-d_6 ices recorded at 9.34 eV (a). Calculated isotopic distribution of $B_{10}D_{18}$ (b) compared with experimental ion signals at *m/z* = 140–146 from irradiated diborane-d_6 ice (c), along with the corresponding TPD profiles (d). The solid blue lines indicate the total spectral fits, and the green shaded regions indicate peak positions assigned to $B_{10}D_{18}$ isomers.

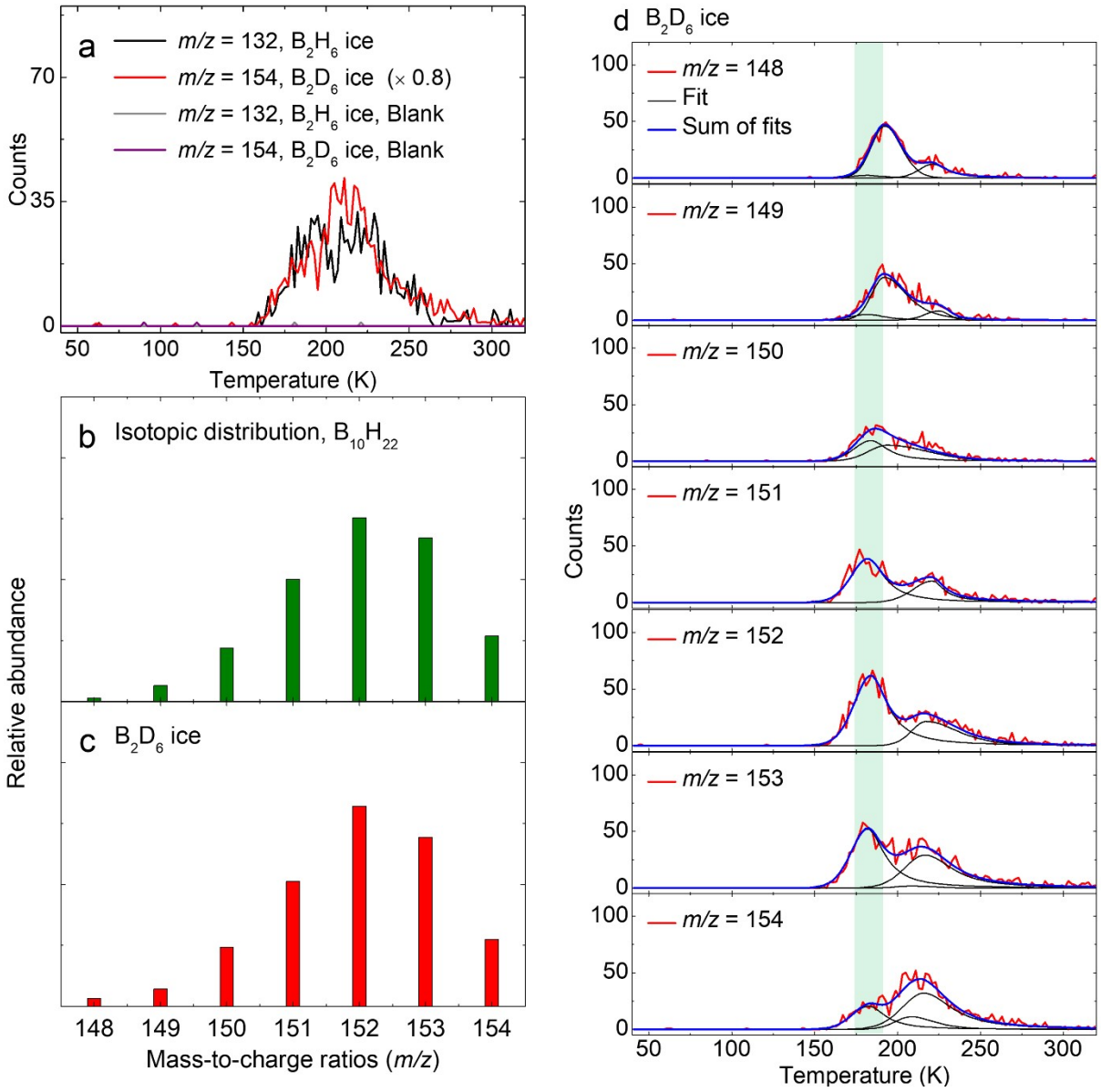

Figure S14. TPD profiles of *m/z* = 132 for diborane ice and *m/z* = 154 for diborane-d_6 ices recorded at 9.34 eV (a). Calculated isotopic distribution of $B_{10}D_{22}$ (b) compared with experimental ion signals at *m/z* = 148–154 from irradiated diborane-d_6 ice (c), along with the corresponding TPD profiles (d). The solid blue lines indicate the total spectral fits, and the green shaded regions indicate peak positions assigned to $B_{10}D_{22}$ isomers.

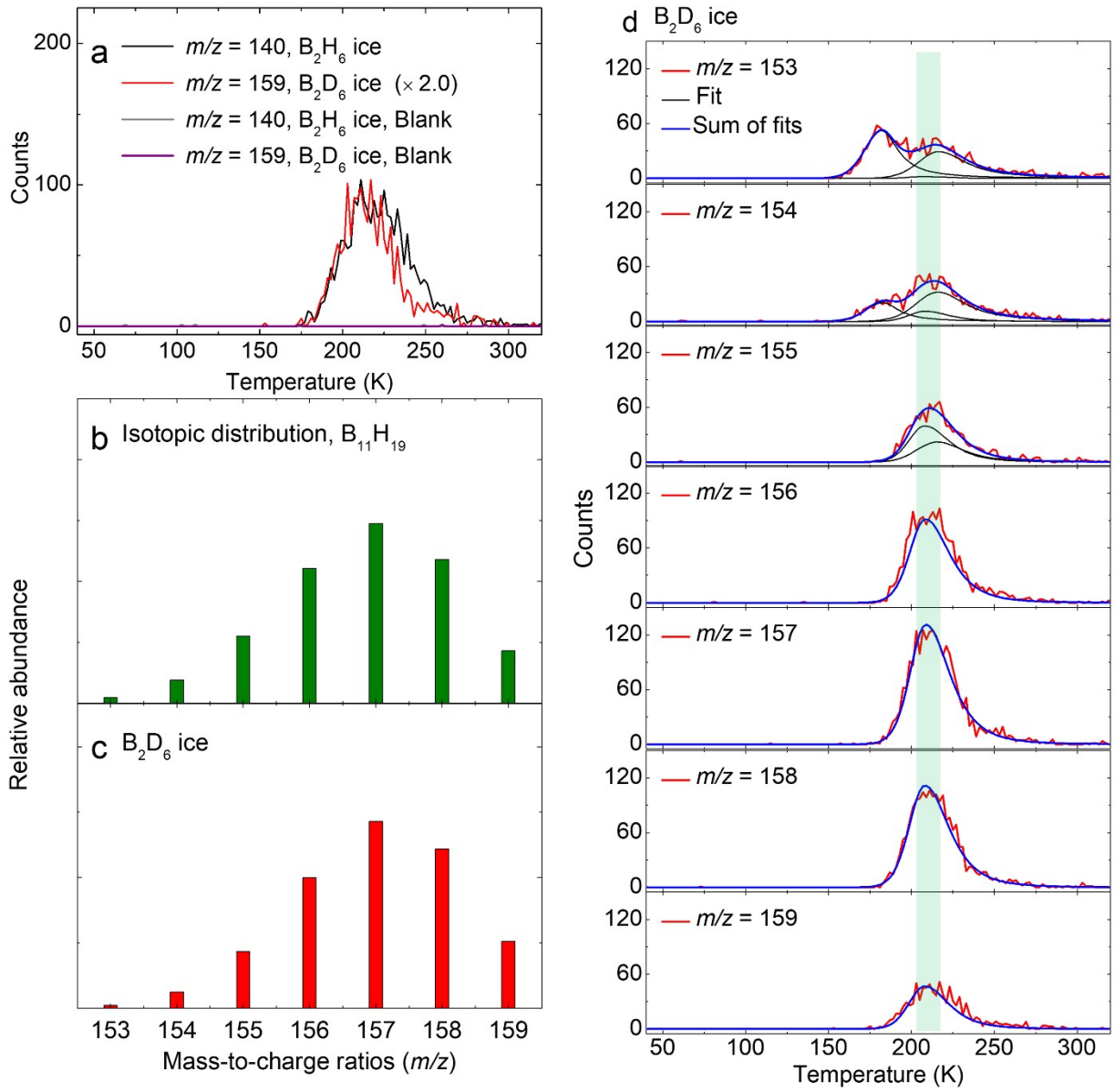

Figure S15. TPD profiles of *m/z* = 140 for diborane ice and *m/z* = 159 for diborane-d_6 ices recorded at 9.34 eV (a). Calculated isotopic distribution of $B_{11}D_{19}$ (b) compared with experimental ion signals at *m/z* = 153–159 from irradiated diborane-d_6 ice (c), along with the corresponding TPD profiles (d). The solid blue lines indicate the total spectral fits, and the green shaded regions indicate peak positions assigned to $B_{11}D_{19}$ isomers.

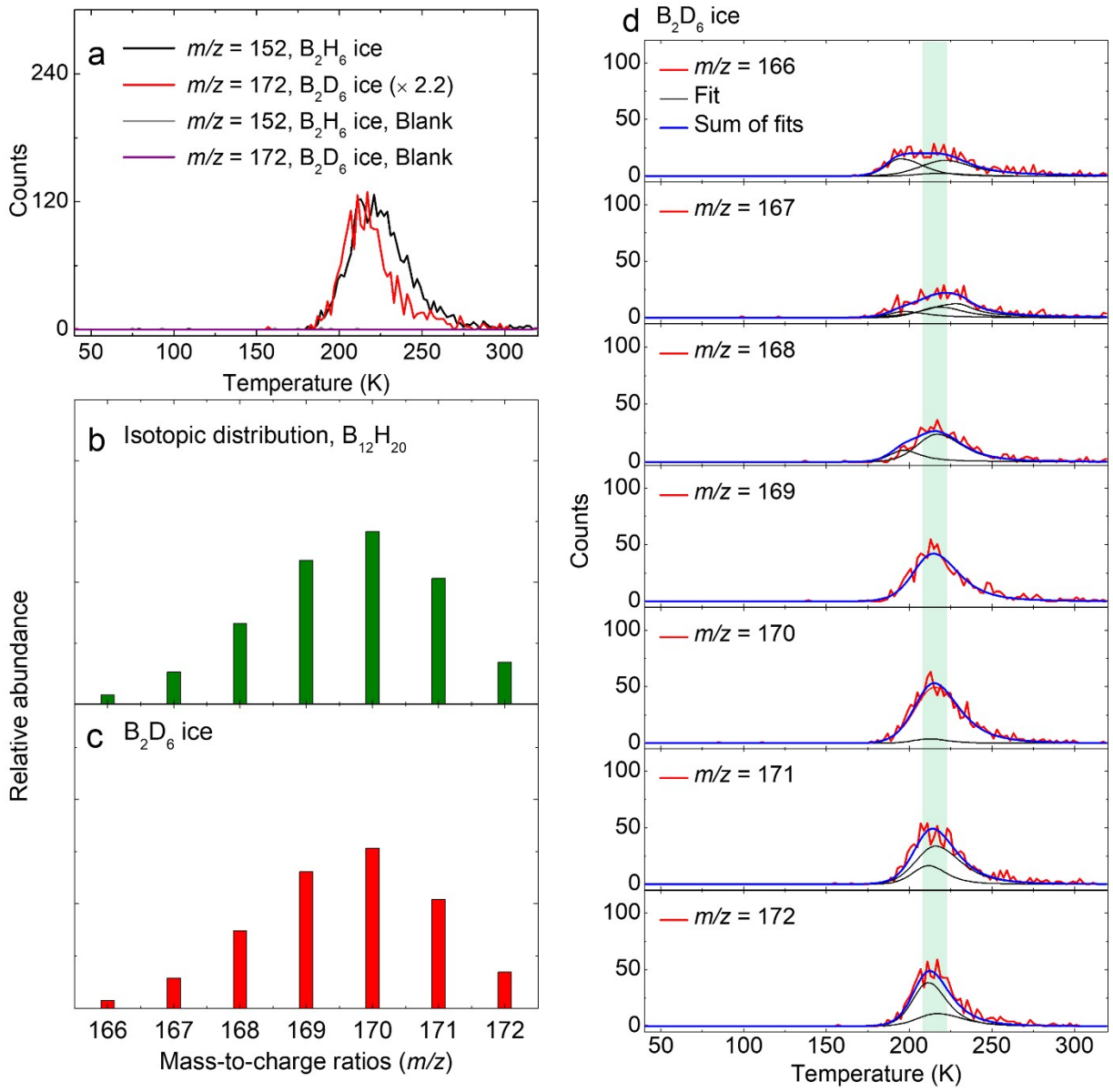

Figure S16. TPD profiles of $m/z = 152$ for diborane ice and $m/z = 172$ for diborane-d_6 ices recorded at 9.34 eV (a). Calculated isotopic distribution of $B_{12}D_{20}$ (b) compared with experimental ion signals at m/z = 166–172 from irradiated diborane-d_6 ice (c), along with the corresponding TPD profiles (d). The solid blue lines indicate the total spectral fits, and the green shaded regions indicate peak positions assigned to $B_{12}D_{20}$ isomers.

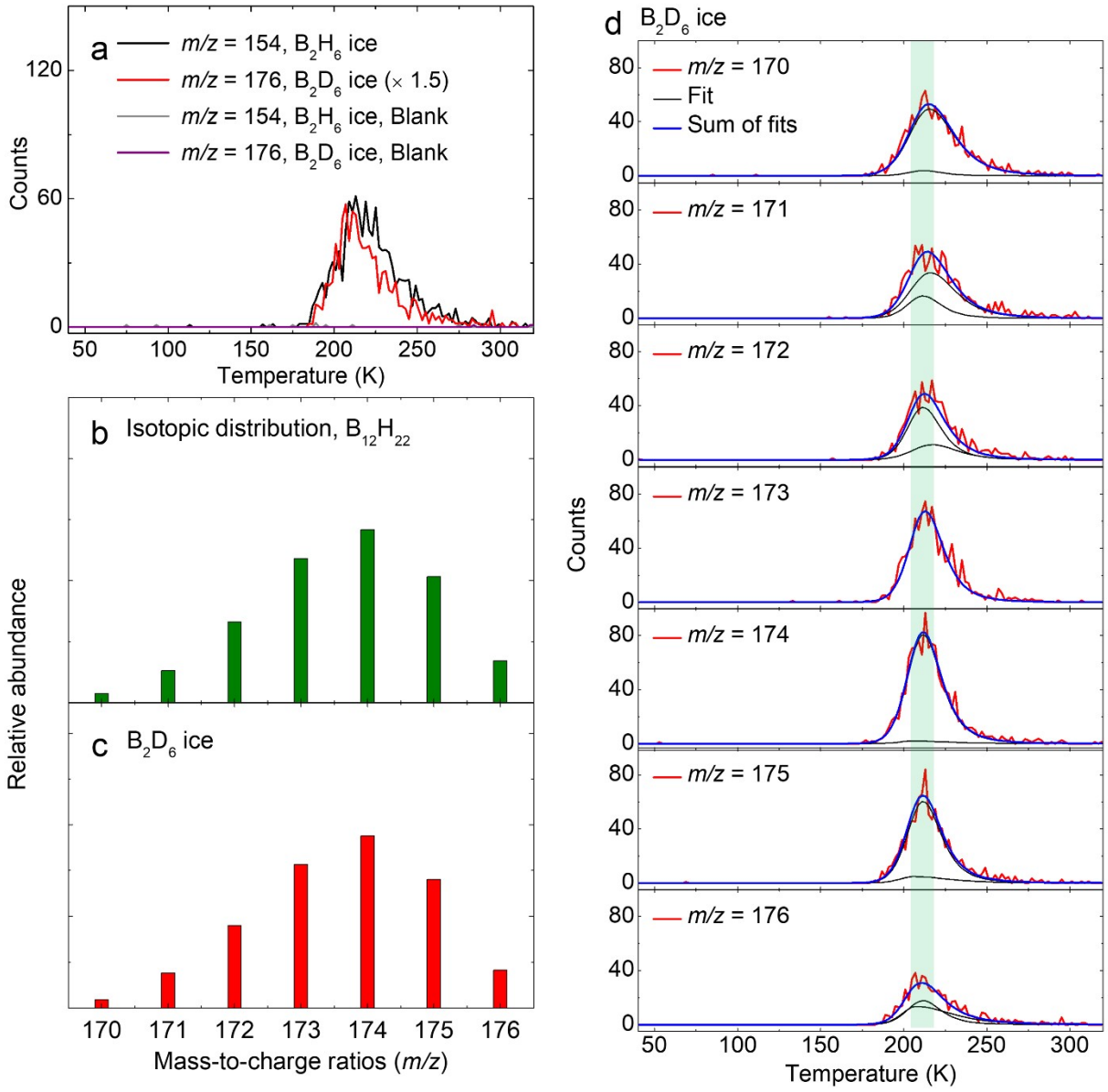

Figure S17. TPD profiles of *m/z* = 154 for diborane ice and *m/z* = 176 for diborane-d_6 ices recorded at 9.34 eV (a). Calculated isotopic distribution of $B_{12}D_{22}$ (b) compared with experimental ion signals at *m/z* = 170–176 from irradiated diborane-d_6 ice (c), along with the corresponding TPD profiles (d). The solid blue lines indicate the total spectral fits, and the green shaded regions indicate peak positions assigned to $B_{12}D_{22}$ isomers.

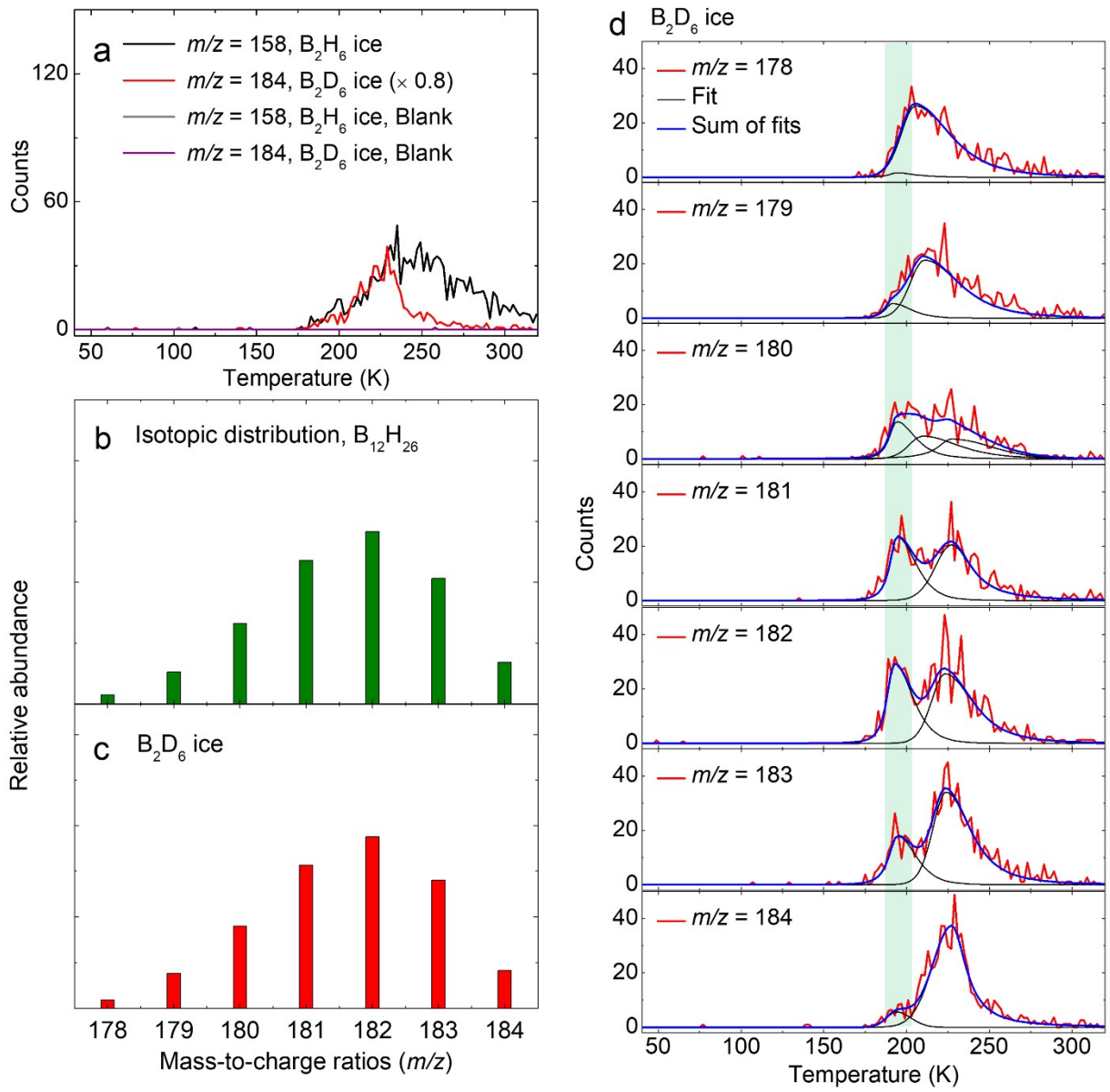

Figure S18. TPD profiles of *m/z* = 158 for diborane ice and *m/z* = 184 for diborane-d_6 ices recorded at 9.34 eV (a). Calculated isotopic distribution of $B_{12}D_{26}$ (b) compared with experimental ion signals at *m/z* = 178–184 from irradiated diborane-d_6 ice (c), along with the corresponding TPD profiles (d). The solid blue lines indicate the total spectral fits, and the green shaded regions indicate peak positions assigned to $B_{12}D_{26}$ isomers.

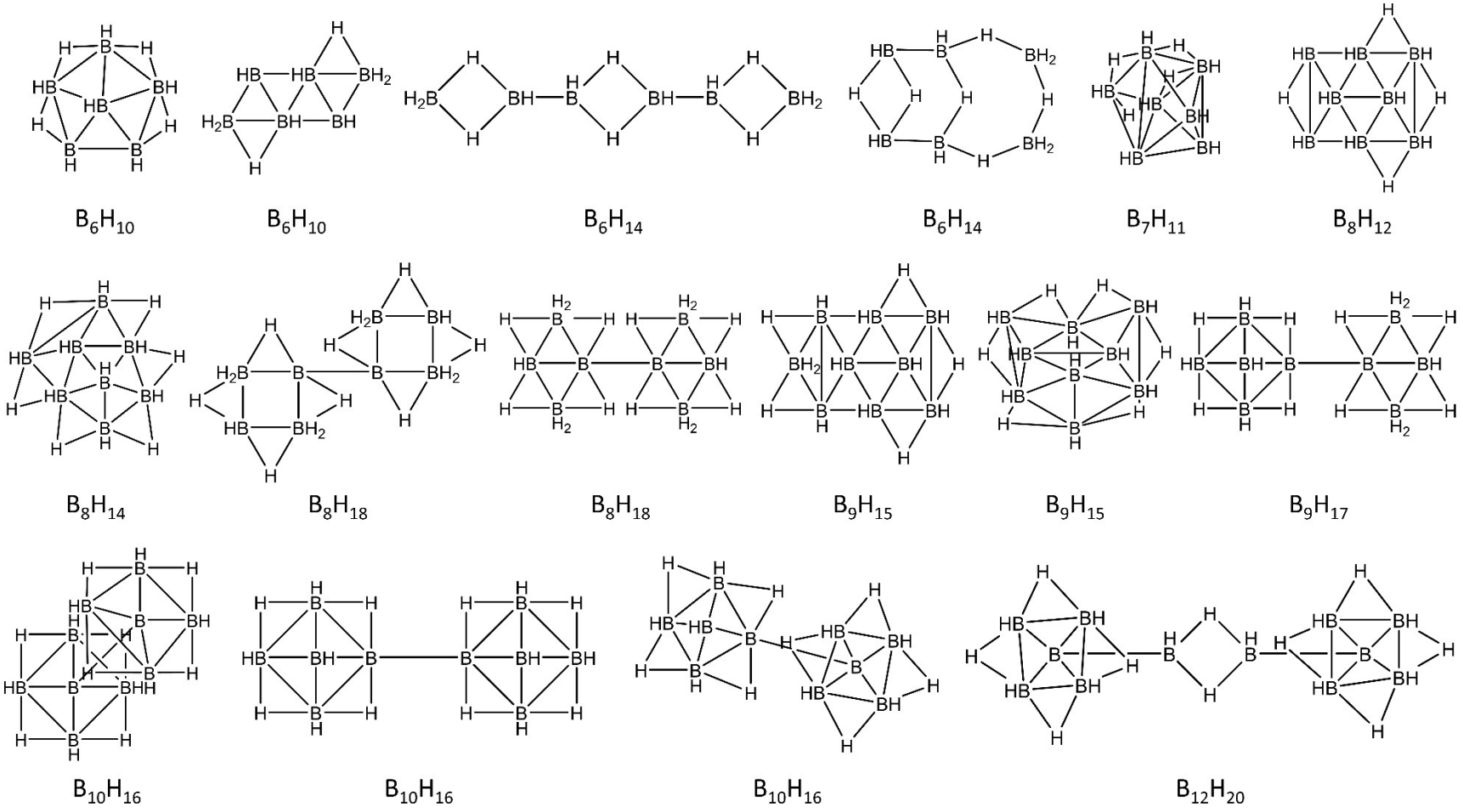

Figure S19. Possible structures of several boranes detected via photoionization reflectron time-of-flight mass spectrometry.

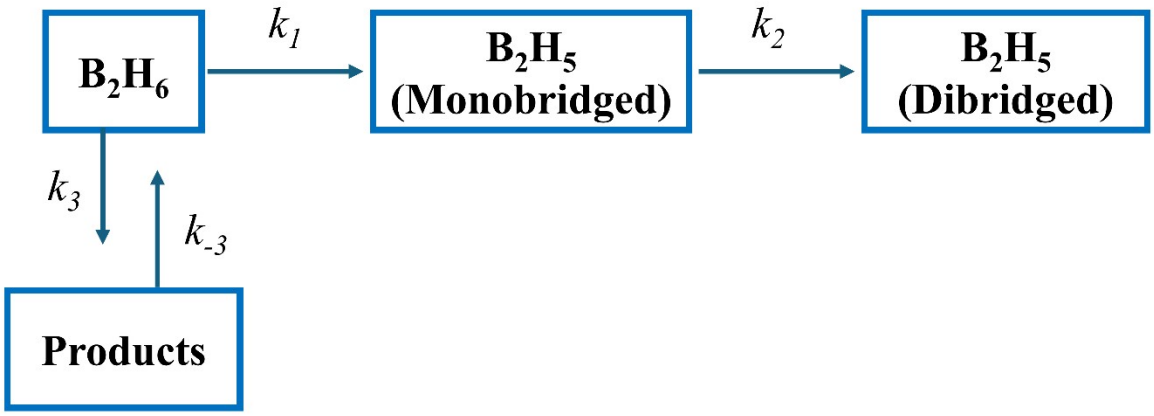

Figure S20. Kinetic reaction scheme employed to fit the temporal evolution of diboranyl (B_2H_5) radicals in the diborane (B_2H_6) ices at 5 K. Infrared absorptions of diborane (B_2H_6), along with monobridged and dibridged diboranyl radicals were fitted with coupled differential equations.

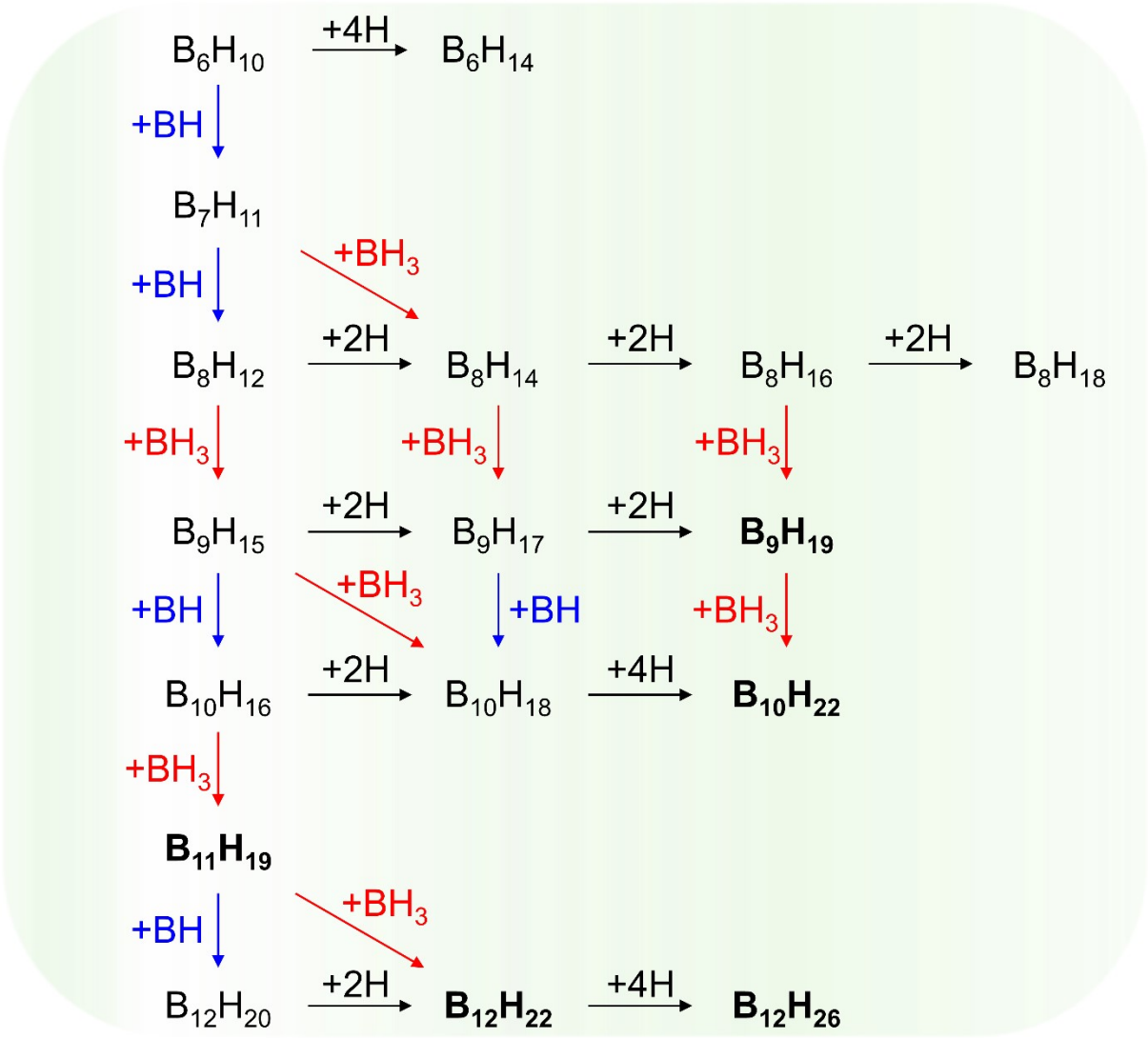

Figure S21. Proposed formation pathways leading to the detected boranes. Black, blue, and red arrows indicate addition reactions involving H atoms, BH radicals, and BH_3 molecules, respectively. Isomers in bold represent species identified for the first time.

Table S1. Absorption peaks observed in diborane (B_2H_6) ice before and after electron irradiation at 40 K.

Pristine B_2H_6 ice, before irradiation (cm^{-1})	Previous measured absorptions of B_2H_6 in crystal phase (cm^{-1})[6]	Assignment[6]
3655	3653	$\nu_3 + \nu_{16}$
3633	3632	$\nu_2 + \nu_3 + \nu_{10}$
3603	3602	$\nu_8 + \nu_{15}$
2760	2755	$\nu_3 + \nu_{17}$
2731	2729	$\nu_7 + \nu_{13}$
2710	2709	$\nu_6 + \nu_{14}$
2616	2624	$2\nu_5 + \nu_{14}$
2600	2597	ν_8
2581	2586	ν_{11}
2525	2522	$\nu_{10} + \nu_{14} + \nu_{18}$
2507	2510	ν_{16}
2328	2364	$\nu_4 + \nu_{17}$
2099	2070	$\nu_3 + \nu_{12}$
2081	2070	$\nu_{12} + \nu_{18}$
1990	1991	$\nu_9 + \nu_{15}$
1880	1880	ν_{13}
1847	1845	$\nu_5 + \nu_{15}$
1828	1826	$\nu_7 + \nu_{14}$
1689	1688	$\nu_5 + \nu_7$
1578	1585	ν_{17}
1163	1173	ν_3
1152	1159	ν_{18}
967	967	ν_{14}
New absorption after irradiation (cm^{-1})	**Calculated anharmonic frequency (cm^{-1}) at the B3LYP/6-311G** level[7]**	**Assignment[7,8]**
2501	2505	ν_4 (monobridged B_2H_5 radical)
2129	2142	ν_4 (dibridged B_2H_5 radical)
2050	2059	$\nu_7 + \nu_{11}$ (dibridged B_2H_5 radical)
1958	1969	$\nu_8 + \nu_{10}$ (monobridged B_2H_5 radical)
1779	1782	$2\nu_{10}$ (monobridged B_2H_5 radical)
1551	1582	$2\nu_{12}$ (dibridged B_2H_5 radical)
1541	1558[a]	ν_6 (monobridged B_2H_5 radical)
1516		asym in-phase motion of H atom (B···H···B (bridged hydrogen))

1511	1524	$2\nu_{12}$ (monobridged B_2H_5 radical)
1416	1434	$\nu_{10} + \nu_{14}$ (dibridged B_2H_5 radical)
1339	1359	ν_6 (dibridged B_2H_5 radical)
1061	1080[a]	ν_7 (monobridged B_2H_5 radical)
1032	1036[a]	ν_8 (monobridged B_2H_5 radical)
1008	1013	$\nu_{12} + \nu_{15}$ (monobridged B_2H_5 radical)
920	926[a]	ν_9 (monobridged B_2H_5 radical)
889	893	ν_{10} (dibridged B_2H_5 radical)

[a] Scaled by a factor of 0.9608.[9]

Table S2. Absorption peaks observed in diborane-d_6 (B_2D_6) ice before and after electron irradiation at 40 K.

Pristine B_2D_6 ice, before irradiation (cm^{-1})	Previous measured absorptions of B_2D_6 in crystal phase (cm^{-1})[6]	Assignment[6]
3349	3351	$\nu_1 + \nu_2$
3333	3333	$\nu_1 + \nu_{13}$
3125	3125	$\nu_{11} + \nu_{17}$
2834	2834	$\nu_2 + \nu_5 + \nu_{15}$
2783	2783	$\nu_9 + \nu_{10} + \nu_{16}$
2735	2734	$\nu_1 + \nu_{18}$
2675	2673	$\nu_2 + \nu_{17}$
2634	2650	$\nu_5 + \nu_{17} + \nu_{18}$
2598	2571	$\nu_{12} + \nu_{16}$
2379	2379	$\nu_3 + \nu_{13}$
2178	2178	$\nu_7 + \nu_{13}$
2102	2100	$\nu_7 + \nu_9 + \nu_{15}$
2085	2084	$\nu_3 + \nu_{17}$
1980, 1966	1966	ν_8
1838	1837	ν_{16}
1775, 1763	1759	$\nu_3 + \nu_{18}$
1685	1730	$2\nu_{18}$
1507	1488	ν_2
1477	1476	ν_{13}
1431	1444	$\nu_{14} + \nu_{15}$
1396	1396	$\nu_9 + \nu_{15}$
1317	1317	$\nu_5 + \nu_{15}$
1270	1275	$2\nu_{10} + \nu_{14}$
1190, 1179	1185	ν_{17}
989	985	$\nu_{10} + \nu_{15}$
868	865	ν_{18}
720	718	ν_{14}
New absorption after irradiation (cm^{-1})	**Calculated anharmonic frequency (cm^{-1}) at the B3LYP/6-311G** level[7]**	**Assignment[7]**
1939, 1952	1941, 1946	ν_1 / ν_2 (dibridged B_2D_5 radical)
1828	1819	ν_3 (dibridged B_2D_5 radical)
1581	1590	$\nu_7 + \nu_{10}$ (monobridged B_2D_5 radical)
1530	1549	$\nu_8 + \nu_{10}$ (monobridged B_2D_5 radical)
1169	1169	$\nu_{12} + \nu_{13}$ (dibridged B_2D_5 radical)
1153	1122	ν_6 (monobridged B_2D_5 radical)
1056	1049	ν_6 (dibridged B_2D_5 radical)
1028	1024	$\nu_9 + \nu_{15}$ (dibridged B_2D_5 radical)
821	818	ν_8 (monobridged B_2D_5 radical)

796	771	ν_{11} (monobridged B_2D_5 radical)
755	757	ν_{10} (dibridged B_2D_5 radical)
740	729	ν_9 (dibridged B_2D_5 radical)

Table S3. Experimental conditions of diborane (B_2H_6) and diborane-d_6 (B_2D_6) ices, including ice thickness, irradiation parameters, and VUV photon energy.

Ice	Thickness (nm)	Current (nA)	Irradiation time (s)	Dose (eV/ diborane)	Photon energy (eV)
B_2H_6	950 ± 100	–	–	–	9.34
B_2H_6	950 ± 100	125 ± 5	7200 ± 10	36 ± 5	9.34
B_2D_6	950 ± 100	–	–	–	9.34
B_2D_6	950 ± 100	116 ± 16	7200 ± 10	33 ± 5	9.34

References

1 M. J. Abplanalp, M. Forstel and R. I. Kaiser, *Chem. Phys. Lett.*, 2016, **644**, 79-98.
2 B. M. Jones and R. I. Kaiser, *J. Phys. Chem. Lett.*, 2013, **4**, 1965-1971.
3 A. M. Turner, M. J. Abplanalp, S. Y. Chen, Y. T. Chen, A. H. H. Chang and R. I. Kaiser, *Phys. Chem. Chem. Phys.*, 2015, **17**, 27281-27291.
4 B. E. Gammon, R. S. Genco and M. Gerstein, *A preliminary experimental and analytical evaluation of diborane as a ram-jet fuel*, 1950.
5 D. Drouin, A. R. Couture, D. Joly, X. Tastet, V. Aimez and R. Gauvin, *Scanning*, 2007, **29**, 92-101.
6 J. L. Duncan, D. C. McKean, I. Torto and G. D. Nivellini, *J. Mol. Spectrosc.*, 1981, **85**, 16-39.
7 J. G. Longenecker, A. M. Mebel and R. I. Kaiser, *Inorg. Chem.*, 2007, **46**, 5739-5743.
8 G. Socrates, *Infrared and raman characteristic group frequencies: Tables and charts*, John Wiley & Sons, Ltd., New York, 3rd edn., 2004.
9 *Standard Reference Database Number 101, Release 22, May 2022, Editor: Russell D. Johnson III,* http://cccbdb.nist.gov/, DOI: 10.18434/T47C7Z.